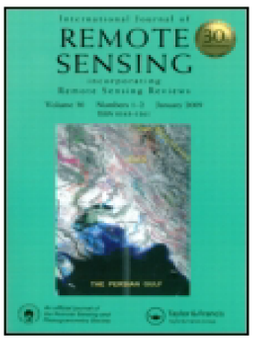

International Journal of Remote Sensing

ISSN: 0143-1161 (Print) 1366-5901 (Online) Journal homepage: http://www.tandfonline.com/loi/tres20

Spatiotemporal mapping of a large mountain glacier from CryoSat-2 altimeter data: surface elevation and elevation change of Bering Glacier during surge (2011–2014)

T. Trantow & U. C. Herzfeld

To cite this article: T. Trantow & U. C. Herzfeld (2016) Spatiotemporal mapping of a large mountain glacier from CryoSat-2 altimeter data: surface elevation and elevation change of Bering Glacier during surge (2011–2014), International Journal of Remote Sensing, 37:13, 2962-2989, DOI: 10.1080/01431161.2016.1187318

To link to this article: http://dx.doi.org/10.1080/01431161.2016.1187318

Published online: 28 Jun 2016.

INTERNATIONAL JOURNAL OF REMOTE SENSING, 2016
VOL. 37, NO. 13, 2962–2989
http://dx.doi.org/10.1080/01431161.2016.1187318

Taylor & Francis
Taylor & Francis Group

Spatiotemporal mapping of a large mountain glacier from CryoSat-2 altimeter data: surface elevation and elevation change of Bering Glacier during surge (2011–2014)

T. Trantow[a] and U. C. Herzfeld[a,b]

[a]Department of Electrical, Computer and Energy Engineering, University of Colorado, Boulder, Boulder, CO, USA; [b]Cooperative Institute for Research in Environmental Sciences, University of Colorado, Boulder, Boulder, CO, USA

ABSTRACT

CryoSat-2 radar altimeter data have been applied to map surface elevations of the Greenland and Antarctic ice sheets, and of Arctic icecaps. In this article we investigate the feasibility of using CryoSat-2 data for spatiotemporal analysis of surface elevation of a large mountain glacier. Bering Glacier, Alaska (which is 8–20 km wide and approximately 80 km long) is selected as a study area because it surges and hence shows short-term elevation changes. The approach includes a correction method, geostatistical analysis, and several methods for error assessment. A time series of digital elevation models (DEMs) is derived for six-month increments from Summer 2011 to Winter 2013/2014. DEMs have, on average, numerical Kriging errors of 1.65 + 3.19 m and Kriging estimation standard deviations of 11.32 + 1.01 m. A crossover analysis with airborne laser altimeter data from the fall months of 2011, 2012, and 2013 produced differences of 5.03 + 13.67 m compared to respective CryoSat-2 data sets. Difference maps are derived from the DEMs and are used to infer dynamical changes associated with the recent surge. In conclusion, CryoSat-2 data can be employed for spatiotemporal mapping of the evolution of surface elevation in Bering Glacier and other mountain glaciers of similar width, while providing key insight into large-scale elevation change over relatively short time periods.

ARTICLE HISTORY
Received 18 August 2015
Accepted 30 April 2016

1. Introduction

Mapping elevation change of glaciers and ice sheets is performed largely by analysis of satellite altimeter data. The European Space Agency's (ESA's) CryoSat-2 satellite makes altimetry measurements using the synthetic-aperture interferometric radar altimeter (SIRAL) instrument, which employs synthetic aperture interferometric principles to improve accuracy and resolution of radar altimeter measurements, especially over sloping terrestrial ice surfaces (Wingham et al. 2006; ESA 2007). CryoSat-2 data have been analysed to investigate surface elevation change of the large ice sheets of Greenland and Antarctica (Helm, Humbert, and Miller 2014). However, it has been

CONTACT T. Trantow trantow@colorado.edu Department of Electrical, Computer and Energy Engineering, University of Colorado, Boulder, Boulder, CO, USA

known since Meier (1984) that ice caps and glaciers outside of the Greenland and Antarctica ice sheets also contribute significantly to sea-level change (such as the large glaciers of Alaska and the Himalayas, the Canadian Arctic and the Patagonian ice fields), and have recently been shown to produce equivalent sea level rise contributions as both ice sheets combined (Gardner et al. 2013). The data analysis base in Gardner et al.'s work is comparatively poor for Alaska, which suggests a high level of uncertainty in the comparative statement and indicates a need for studies of satellite altimetry for large mountain glaciers. This will be undertaken in this article. While CryoSat-2 has been used to study elevation changes of ice caps such as Austfonna (McMillan et al. 2014) and those in the Canadian Arctic and Svalbard (Gray et al. 2015), its usefulness in the study of mountain glaciers remains unknown. This motivates an investigation of the feasibility of mapping elevation and elevation-change of large mountain glaciers from CryoSat-2. There is a lower limit to the size of glaciers that can be studied using spaceborne radar altimetry and one of the objectives of this article is to examine this limit for CryoSat-2. A second motivation comes from the background of different acceleration types encountered in the cryosphere. Understanding glacial acceleration is one of the largest sources of uncertainty in assessment of future sea-level rise, as found by the Intergovernmental Panel on Climate Change (IPCC) in their recent (2013) Assessment Report 5 (Stocker et al. 2013). There are three (Clarke 1987), or four, depending on definition (Truffer and Echelmeyer 2003), types of glacial acceleration, of which the surge phenomenon is the one that has seen the least amount of research (Meier and Post 1969; Raymond 1987; Harrison and Post 2003; Herzfeld, McDonald, and Weltman 2013b).

The Bering–Bagley Glacier System (BBGS) is the largest surge-type system on Earth and the largest glacier system in continental North America (Molnia 2008). The Bering Glacier portion of the BBGS is 8–20 km wide and ~80 km long from the terminus to the Bering–Bagley Junction (BBJ), whereas the Bagley Ice Field varies between 6 and 12 km in width and stretches over 90 km in length from the BBJ to the Columbus Glacier near the Alaska–Canada border (see Figure 1). Bering Glacier has been surging during 2011–2013, i.e. after the launch of CryoSat-2 in April 2010. As a surge-type glacier system, the BBGS undergoes a quasi-cyclic cycle between a long quiescent phase (about 20 years for the BBGS) of normal flow and gradual recession, and a short surge phase (3 years or more for the BBGS) of rapid down-glacier advancement where the glacier exhibits large mass transfers reflected by large elevation changes (Molnia and Post 1995). For Bering Glacier, examples of elevation changes due to mass transfer between 2010 and 2011 were 20–40 m and 50–70 m (Herzfeld et al. 2013c). To analyse elevation changes during a surge, altimeter data cannot be accumulated over a long time frame, which in turn will necessitate an analysis of the minimal amount of observations required for elevation mapping. Therefore, analysis of CryoSat-2 data for Bering Glacier will provide a robust test case. If it is possible to derive geophysically useful maps from CryoSat-2 data for the Bering Glacier surge, then this will indicate that CryoSat-2 data can be used for analysis of changes in other large mountain glaciers as well.

Lee et al. (2013) analyse satellite radar altimeter data from the Ocean Topography Experiment (TOPEX/Poseidon) and the Environmental Satellite (ENVISAT) missions over Bering Glacier; however, the sparse distribution of ground tracks only permits along-track elevation-change calculation in three widely separated areas. The improved coverage

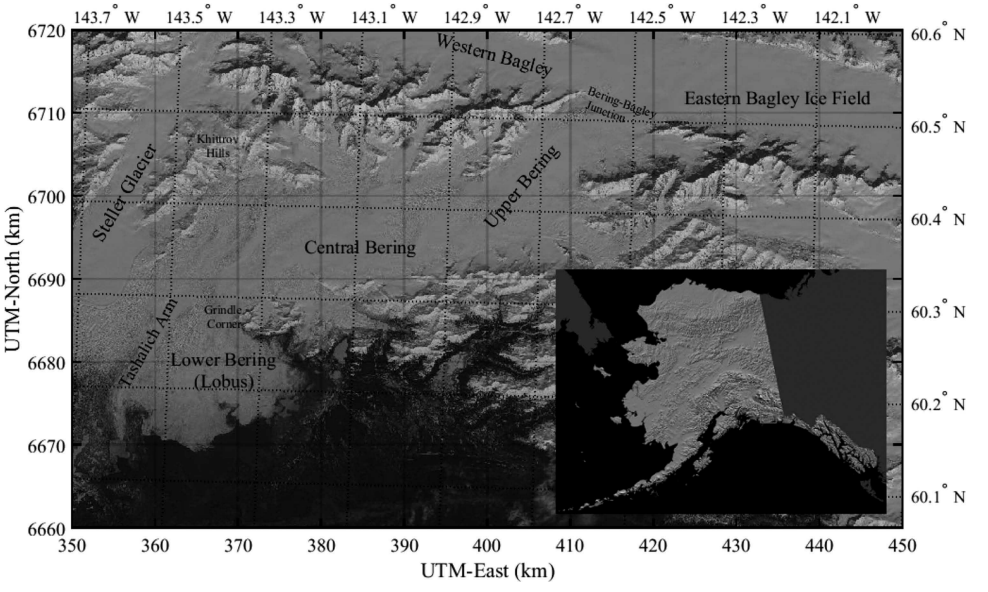

Figure 1. The Bering–Bagley Glacier System. Labelled are the key locations on and near the BBGS. Relative coordinate references are displayed for the Universal Transverse Mercator (UTM) coordinate system (solid grey lines) and geographic coordinate system (dotted black lines). Background image from LandSat-8 acquired on 28 April 2013. Reference image in lower right: US Geological Survey Map I-2585.

facilitated by the interferometric measurements of CryoSat-2 may allow estimation of gridded elevation models.

The fundamental objective of this article is to determine the validity of using CryoSat-2 measurements in the study of large glaciers in mountainous regions. This study utilizes CryoSat-2 level 2 data to derive seasonal digital elevation models (DEMs) of Bering Glacier from 2011 to 2014. The geostatistical methods of variography and Kriging are employed to construct 200 m resolution grids describing the glacier surface topography. A full error analysis is conducted that includes the estimation standard deviation of Kriging along with estimates of the noise levels in the data and its propagation through the Kriging algorithm. Results from airborne observations are used to estimate uncertainties in the CryoSat-2 data. Difference maps are then derived and used to analyse large-scale mass transfers associated with the recent surge.

2. CryoSat-2 SIRAL data

2.1. *Measurement concepts*

The European Space Agency's CryoSat-2 mission is an Earth Explorer Mission launched on 8 April 2010 into a 717.2 km altitude orbit with 92° inclination. CryoSat-2's geographic coverage extends to 88° N/S, which facilitates study of polar regions. The repeat period is 369 days, with a 30-day sub-cycle. The main payload of CryoSat-2 is the SIRAL instrument, a new type of sensor designed to collect altimeter data in three modes: Low-resolution mode (LRM), synthetic aperture radar (SAR) mode, and synthetic-aperture

interferometric (SARIn) mode. Data acquisition is conducted using geographic masks, which have been determined by ESA in communication with the CryoSat-2 Principal Investigators. Alaska is entirely within the SARIn mode mask, which is ideal for studies of elevation changes of the BBGS during the surge cycle.

In LRM, the SIRAL operates like a conventional pulse-limited radar altimeter. In the other two modes, SAR-type formation and processing of the signal is employed to increase resolution in the along-track direction to 250 m (approximately 300 m in the Bering Glacier area). Over critical areas of the margins of the ice sheets, SIRAL data are collected in SARIn mode, which is the most interesting capability of the SIRAL instrument. Designed to better capture surface elevation in sloping areas, SIRAL receives data using two antennas, which facilitates identification of ground returns off nadir (which is impossible with conventional altimetry) (Wingham et al. (2004), 2006); Drinkwater et al. (2004); ESA (2007)). The 250 m spacing is an improvement over the European Remote Sensing satellites (ERS-1/2) radar altimeter data spacing, which achieved between 335 m and 4 km spacing in the geodetical phase (Bamber, Ekholm, and Krabill 2001), whereas data from the Geoscience Laser Altimeter System (GLAS) from the National Aeronautics and Space Administration's (NASA's) Ice, Cloud and land Elevation Satellite (ICESat) have an along-track spacing of 173 m (Zwally et al. 2005; Schutz et al. 2005). In the across-track direction, the area from which the energy is returned for SIRAL is as large as the footprint, which is up to 15 km, depending on surface roughness.

The SIRAL instrument is a 13.6 GHz normal-incidence radar altimeter with a single transmit unit and two receive chains, including two slightly elliptical antennas elongated in along-track direction and offset by 1.17 m in across-track direction. In SARIn mode, bursts of 64 pulses of the same 18.182 PRF are transmitted, but at a slower burst repetition rate than for the SAR mode, and both receiving chains are employed. The processing is described in detail in Wingham et al. (2006). In essence, since the two antennas are spaced 1.17 m in across-track direction, the angle of arrival can be measured in addition to the slant range, which allows to determine the ground location of the point of first return, in the across-track direction, in addition to elevation at that point. As a result, there is one point per along-track location, but the ground location is not necessarily at nadir.

2.2. *Data processing type*

The data type utilized in the analyses of this article is the level-2 (L2) data product of release Baseline B provided by ESA (Bouffard 2015). The L2 data product is the data type that most users will employ for geophysical studies and the data product that is distributed to the user community at large. To produce L2 data, the received signals are processed using the Point of Closest Approach (POCA) and related lobe for elevation determination. Returns beyond the POCA also exist, but are weaker and not always unambiguous (ESA 2007). Compared to Baseline-A CryoSat-2 L2 data, Baseline-B L2 data are derived by application of an improved determination algorithm for the POCA. Baseline-A data show many CryoSat-2 tracks with ground points in straight lines, whereas as a result of the better POCA algorithm the data processed in Baseline B show an across-track scattering to the uphill side of the theoretical ground track over sloping glaciers. The main difference between Baseline A to Baseline B (January 2012) is

the use of finer gate spacing in Baseline B, which results in a truncation of the trailing edge of the waveform (Bouffard 2015).

2.3. *Sources of error and uncertainty*

In the process of measuring, processing, and interpolating altimeter data, sources of errors and uncertainties exist at every step. The lowest-level errors occur at the engineering level. In satellite altimetry, the engineering-level data are typically collected pre-launch in airborne campaigns and in early satellite revolutions of the Earth, at which time corrections are undertaken by the space agency (ESA).

The next group of uncertainties can be addressed at the processing levels, when different data products are derived. In addition to the L2 data product that is used in this study, ESA provides earlier levels of data, such as level L1b data. We originally processed the Bering Glacier CryoSat-2 for Baseline-A data and reprocessed after Baseline-B data were released, which resulted in significant improvements of elevation and elevation-change maps.

Galin et al. (2013) analyse across-track ground-point determination errors in ocean surface data and conclude that the instrument performance considerably exceeds that needed for the accurate determination of height over the sloping surfaces of the continental ice sheets. In consequence, the remaining across-track slope error is not deemed a problem by Galin et al. (2013). Alternative forms of SIRAL L2 data processing are described by Helm, Humbert, and Miller (2014) and applied for mapping surface heights of the Greenland and Antarctic ice sheets. These authors employ different processing methods to derive level-2 data of the same type as ESA's L2 data – one point per along-track location.

In contrast to POCA-based level-2 data, which result in one point per along-track location, Gray et al. (2013) explore the extent to which the phase of the returns can be used to map height in the time-delayed footprints beyond the POCA, creating an experimental swath-processing method. The advantage of swath processing is that coverage of a survey area by CryoSat-2 data is greatly improved, as there are more resultant data points. To date, swath processed data are a topic of research and are not yet a generally available CryoSat-2 data product. Gray et al. (2013, 2015) apply this swath processing method to analyse surface elevation change from SARIn mode data for the ice caps of the Canadian Arctic on monthly and yearly timescales and compare results to airborne laser scanning altimeter data.

In our article, the last group of errors and uncertainties is examined in depth: Errors and uncertainties resultant from spatial data analysis and grid estimation will be analysed, using several approaches, including a method for numerical error propagation through the Kriging equations that is mathematically derived here (but was applied in an earlier paper (Herzfeld, Lingle, and Lee 1993)). Results of our analysis will then be evaluated using cross-over differences between CryoSat-2 surface heights and surface heights from airborne laser altimetry (Section 7). These steps are aimed at establishing that CryoSat-2 L2 data can be used to map ice-surface elevations and elevation changes for large mountain glaciers and glacier systems. The processing and correction methods derived in our article will also be applicable to other CryoSat-2 level 2 products, such as those derived in Helm, Humbert, and Miller (2014).

For calculation of the DEMs, a 200 m grid cell size was selected to facilitate numerical modelling experiments at a sufficiently high resolution that will resolve specific glacier dynamic processes. Here, the relatively high grid resolution aids the contouring process. Notably the grid size does not influence the vertical accuracy of the resultant DEMs, because the Kriging standard deviation as well as the numerical error (see Section 8) are calculated as a value at a given point. In consequence, a DEM sub-sampled at, say, 1 km grid resolution from the DEMs presented at 200 m will be identical with a DEM calculated at 1 km. In other words, maps derived from small grid cells are just as reliable as maps built on larger grid cells, and in addition, have the advantages of better spatial resolution. Therefore, the grid size, unless too large, is not a source of uncertainty.

3. Methods

3.1. *Determination of observation time interval required for DEM calculation*

Because rapid and large elevation changes are characteristic during a surge, frequent observation and mapping of surface elevation is desirable when documenting elevation changes during a surge. However, CryoSat-2 data, while being acquired continuously, do not yield sufficient spatial coverage to allow monthly elevation surveys as would be ideal for analysis of elevation change during a surge. In other words, the sparse survey pattern of CryoSat-2 measurements for a single month, over the entire glacier, will result in estimated standard deviation errors (see Section 6.1) that are too high for reliable geophysical interpretations.

Figure 2 shows the coverage of the CryoSat-2 data for three different time intervals. Using data from six-month time intervals, coverage is sufficient for deriving DEMs that

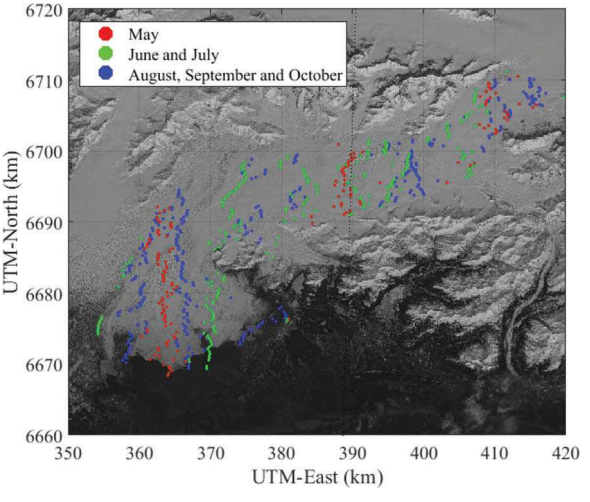

Figure 2. Typical CryoSat-2 ground tracks over Bering Glacier, Alaska for time intervals of different lengths. Red points represent measurements the CryoSat-2 instrument made during the month of May 2013; green during June and July 2013; and blue during August, September, and October 2013. Survey patterns from additional time periods can be seen in Figures 7 and 8. Background image from LandSat-8 acquired on 28 April 2013.

span the entire glacier and are beneath a reasonable error tolerance, which is justified in Section 8 on error analysis.

Between launch and February 2011, only engineering-type data were collected and no L2 (Baseline B) elevation data were produced. Therefore, CryoSat-2 altimeter data useful for geophysical research start in February 2011. We use three years of data from May 2011 to April 2014, divided into six 6-month intervals: May 2011 to October 2011 (Summer 2011), November 2011 to April 2012 (Winter 2011/2012), May 2012 to October 2012 (Summer 2012), November 2012 to April 2013 (Winter 2012/2013), May 2013 to October 2013 (Summer 2013), and November 2013 to April 2014 (Winter 2013/2014). These divisions correspond to the accumulation/ablation balance measured in 2011 on Bering Glacier where during the months of May–October the glacier experienced noticeable ablation whereas during the months of November–April, ablation was relatively stagnant (Tangborn 2013).

It should be noted that the orientation of the flight track relative to the glacier geometry affects the data coverage in a given time frame. A flight track along the glacier length will produce more measurements of the glacier surface per pass compared to a flight track oriented transverse to the glacier.

3.2. *Variography and Kriging*

3.2.1. *Variograms*

The geostatistical methods of spatial structure analysis using variography and grid estimation using ordinary Kriging are applied to derive DEMs of the ice surface of Bering Glacier (Matheron (1963); Journel and Huijbregts (1989); Herzfeld (1992), 2004)). We briefly review the formulation of variography and Kriging since it is utilized in the error analysis (Section 8). The underlying concept of geostatistics is that of the regionalized variable. A regionalized variable $z(x)$ is a spatial variable (a variable defined for spatial locations $x \in \mathbb{R}^2$ or $\mathbb{R}^3$, the two- or three-dimensional space of real numbers) with a transitional behaviour between deterministic and random states. CryoSat-2 altimeter data $z_i(x)$, where $i = 1, \ldots, n$, on $z(x)$ may be considered a realization of a spatial random function $Z(x)$ for $x \in$ D with the property that $(Z(x) - Z(x+h))$ is a second order stationary random function for a fixed separation distance $h \in \mathbb{R}^2$ such that $x, x+h \in$ D, where the glacier region D is a subset of $\mathbb{R}^2$. This property is called the *intrinsic hypothesis*.

Under the intrinsic hypothesis, the *(semi-) variogram*

$$\gamma(h) = \frac{1}{2} E\left[Z(x) - Z(x+h)\right]^2 \tag{1}$$

exists and is finite, where γ measures the spatial continuity between points separated by a distance h (E denotes the mathematical expectation) (Matheron 1963; Journel and Huijbregts 1989). In practice, an experimental variogram is calculated from the data set on the domain D, according to the formula

$$\gamma_{\text{exp}}(h) = \frac{1}{2n} \sum_{i=1}^{n} \left[z(x_i) - z(x_i + h)\right]^2, \tag{2}$$

where $z(x_i)$ and $z(x_i + h)$ are samples taken at locations $x_i, x_i + h \in D$, respectively, where n is the number of pairs separated by h. Kriging is best performed in an orthogonal coordinate system with units in meters (such as the Universal Transverse Mercator (UTM) coordinate system), because for each estimation multiple distance searches are carried out. Hence, all resultant maps are presented in the UTM coordinate system. Figure 1 relates UTM coordinates to geographic coordinates for comparison with other work on Bering Glacier.

3.2.2. *Kriging*

Estimation of surface elevation at a given location $x_0 \in D$ is performed by Kriging. Kriging, named after pioneering geostatistician Danie Krige, is a family of least-squares-based estimators. The general linear estimator is

$$Z_0^* = a_0 + \sum_{i=1}^{n} a_i Z(x_i) \text{ with } a_i \in \mathbb{R}, \tag{3}$$

where weights a_i are determined by a minimum variance criterion

$$\min\left(E\left[Z_0^* - Z_0\right]^2\right) \tag{4}$$

and with respect to unbiasedness conditions $E[Z_0^* - Z_0] = 0$, where $Z_0 = Z(x_0)$ is the unknown true value in the estimation at x_0 and $Z_i = Z(x_i)$ for measurement locations x_i where $x_0, x_i \in$ D, for $i = 1...n$.

The salient concept in Kriging is to replace the unknown covariances that occur in the minimization algebra by known variogram values (for mathematical formulation, see Herzfeld (1992)). The variogram values are taken from a variogram model, which is fitted to a so-called experimental variogram, calculated from the data. Mathematically, this substitution is justified by the intrinsic hypothesis. Minimization of the estimation variance yields a matrix equation (or n conditions). The unbiasedness conditions depend on the information available on the expectation of $Z(x)$. This leads us to the method of Ordinary Kriging (OK), which assumes an unknown but constant expectation $0 \neq E = E[Z(x)]$ for all $x \in D$, resulting in an unbiasedness condition that requires

$$\begin{aligned} \sum_{i=1}^{n} a_i &= 1 \\ a_0 &= 0 \end{aligned} \quad . \tag{5}$$

A solution satisfying the n conditions from Equations (3) and (4), and the unbiasedness condition (5) is obtained from a system of $(n + 1)$ linear equations (Kriging system), using a Lagrange parameter λ:

$$\begin{pmatrix} \gamma_{1,1} & \cdots & \gamma_{1,n} & 1 \\ \vdots & \ddots & \vdots & \vdots \\ \gamma_{n,1} & \cdots & \gamma_{n,n} & 1 \\ 1 & \ldots & 1 & 0 \end{pmatrix} \begin{pmatrix} a_1 \\ \vdots \\ a_n \\ \lambda \end{pmatrix} = \begin{pmatrix} \gamma_{0,1} \\ \vdots \\ \gamma_{0,n} \\ 1 \end{pmatrix}, \tag{6}$$

where

$$\begin{aligned} \gamma_{0,i} &= \gamma(|x_0 - x_i|), \\ \gamma_{i,j} &= \gamma\left(\left|x_i - x_j\right|\right), \\ i,j &= 1,\ldots,n. \end{aligned} \tag{7}$$

The matrix in (6) is the *(ordinary) Kriging matrix*.

The Kriging Equation (6) has a unique solution, if positive-definite variogram models are used. Such models include the Gaussian model (Equation 8), which is employed in this analysis.

4. Variogram analysis

4.1. *Experimental variogram*

Variogram analysis is described for the six-month data set with the best glacier surface coverage (Summer 2012). To calculate the experimental variogram a lag spacing (i.e. the separation distance bin size) of 300 m is used, which matches the approximate average along-track spacing of CryoSat-2 data in the study region. Variogram values are calculated for a total of 23 distance bins, spanning 300 m $\times$ 23 $=$ 6900 m. A search radius of 6900 m is used when Kriging and is thus the maximum extent of the spatial relationship that is needed. When Kriging, we use 10 data points to weight the estimation at each grid node. The maximal distance from some 200 m-by-200 m grid node on Bering Glacier to the 10th closest data point is 6891.2 m (occurring in the Winter 2012/2013 data set). Thus we only require an expression of the spatial relationship of surface elevation (variogram) up to 6900 m.

Variogram models are then fitted to the experimental variograms. Variogram models are characterized by their function type and other model parameters (which ensures that the positive definiteness condition of Kriging is satisfied and hence that the inversion step in the Kriging problem has a unique solution, see Herzfeld (2004)). The Gaussian model is best suited for Kriging of glacier surfaces at a scale that does not resolve crevasse fields (Herzfeld, Lingle, and Lee (1993)). The Gaussian variogram model is given by the equation

$$\gamma_{\text{gau}}(h) = c_0 + c_1\left(1 - \mathrm{e}^{\frac{-h^2}{a^2}}\right), \tag{8}$$

where c_0 is the nugget, a is the range and $c_1 - c_0$ is the sill. The *nugget effect* occurs when $c_0 \neq 0$ and is a consequence of noise in the measurements. Therefore, estimates of the noise level for the CryoSat-2 data can be estimated by finding the nugget value associated with each data point, as is done in Section 8 on error analysis. The sill is the variogram value at which the correlation between $Z(x)$ and $Z(x+h)$ ceases to exist and the corresponding lag value a at this point is called the range.

A least-squares fit is calculated for the experimental variogram for Summer 2012. The Summer 2012 experimental variogram, seen as circles in Figure 3, appears unbounded within our search radius of 6900 m. Alternate studies have used power functions of order less than or equal to 2 to fit unbounded variograms (Curran 1988; Biau et al. 1999), but here we use a Gaussian fit with a range (and corresponding sill) that is greater than the search radius. Variogram modelling is robust to outliers and consequently the variograms before and after filtering (Section 4.2) are effectively the same.

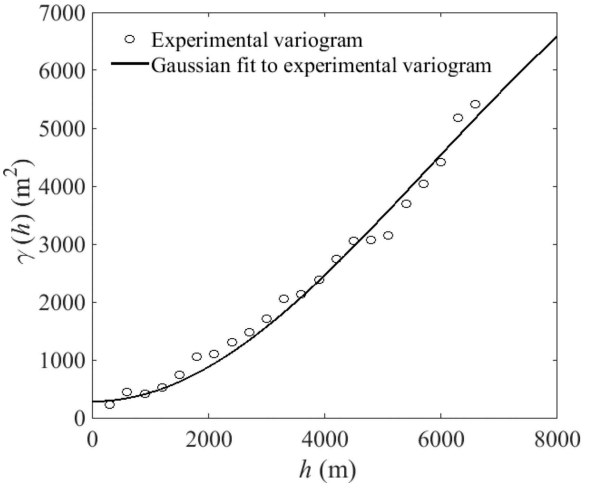

Figure 3. Experimental variogram for Summer 2012 CryoSat-2 elevation measurements and the Gaussian fit to that data. The variogram parameters from this Gaussian fit are used when Kriging every data set in this study: nugget = 289 m^2, sill = 10,486 m^2, range = 14,133 m.

4.2. *Filtering*

To remove outlier points, a double pass filter is used that exploits the spatial relationship of elevation given by the experimental variogram in each data set. For every point x_j in the data set D, a weighted elevation difference measure $\zeta(x)$ is calculated using data within a radius r. Because the experimental variogram is a discrete measure, separation distances fall into bins the size of the lag spacing l (Herzfeld 2002). The algorithm thus uses the first $\frac{r}{l}$ experimental variogram values $\left(\gamma_{\text{exp}}(h)\right)$, where r is chosen to be a multiple of l. Finally, the elevation distance weights Γ are simply the inverse of $\gamma_{\text{exp}}(h)$ for $h = l, 2l, \ldots, r$. In functional form: for each $x_j \in$ D,

$$\zeta(x_j) = \Gamma(\Delta x) \sum_{i=1}^{n} \left| z(x_j) - z(x_i) \right|, \tag{9}$$

with

$$\frac{1}{\Gamma(\Delta x)} = \begin{cases} \gamma(l): & 0 < \Delta x \leq l \\ \gamma(2l): & l < \Delta x \leq 2l \\ \vdots & \\ \gamma(r): & r - l < \Delta x \leq r \end{cases},$$

where $z(x)$ is the elevation at x and $\Delta x = |x_j - x_i| \leq r$. A point x_j is considered an outlier if $\zeta(x_j)$ is greater than a heuristically determined tolerance.

In this analysis, a lag spacing of $l = 300$ m is used along with an initial radius of $r = 1500$ m. A tolerance of 100 m was used, which was derived by analysing elevation differences within the given radius (r) that can be expected based on realistic surge-induced elevation changes and the glacier geometry (Herzfeld et al. 2013c; Trantow 2014). $\gamma_{\text{exp}}(h)$ values are given by the experimental variogram calculations for each

individual data set. Outliers determined after the first pass of this algorithm on the Summer 2013 data set are visualized in Figure 4(b)).

After the first pass, the algorithm identifies outlier points as defined above but also flags points that may be valid (such as the orange points in the upper glacier in Figure 4 (b), where the algorithm has determined that these few points, around 900 m in elevation, are outliers when in reality most points in that vicinity are 900 ± 100 m in elevation). These points are flagged due to their proximity to a significant number of true outliers thus giving them higher elevation difference measures. Therefore, a second pass through the filter is employed where the original data set D is measured against an adjusted data set D\S (all points in D that are not in S), where S is the set of all points x_j such that the associated elevation distance measure $\zeta(x_j)$ is greater than the tolerance in first pass through the algorithm. The radius r is increased slightly on account of the smaller data set, and the final data set used in DEM generation is determined after the second iteration of the filtering algorithm (Figure 4(c,d)).

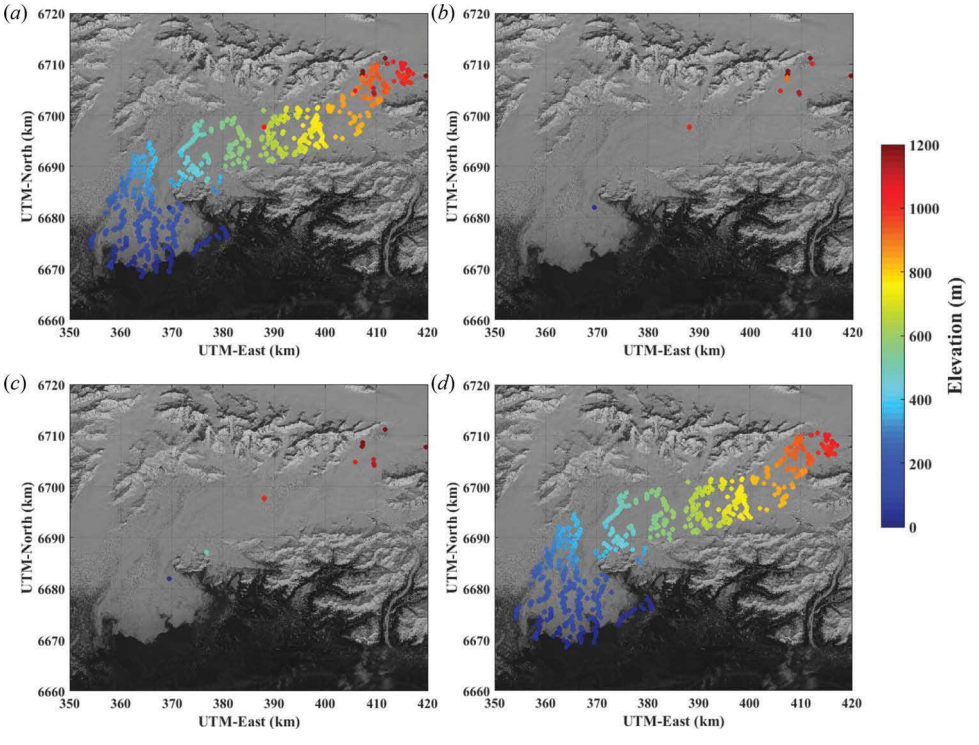

Figure 4. Results after each stage of the elevation outlier algorithm. (a) Original unfiltered CryoSat-2 L2 data set for Summer 2013. (b) Outlier points determined after the first pass of the algorithm. (c) Outlier points determined after the second pass of the algorithm. (d) Final filtered data set used for creating a digital elevation model of the Summer 2013 season. Background image from LandSat-8 acquired on 28 April 2013.

5. Calculation of digital elevation models

Ordinary Kriging is used for the interpolation of the CryoSat-2 data over Bering Glacier, because of the geophysical track-line distribution that is typical of satellite altimeter data, with characteristic high along-track data density and large gaps between tracks. The OK method compensates for linear drift components and does not assume second-order stationarity of the observations. A higher-order method, such as Universal Kriging (UK), is usually numerically less stable and likely creates artefacts (Herzfeld 1989, 1992). The relationship between the search radius and the length scale of surface trends determine whether OK or UK is used. To check this, we calculated the difference between the variogram and the residual variogram over the relevant length scales. These two values differ by $<0.1\%$ for $0 < h \leq 2100$, and $<1\%$ for $2100 < h \leq 6900$. Since this difference is negligible in our study, OK should be used for DEM calculation.

To best exploit the CryoSat-2 data, which follow satellite ground tracks with some scattering, we use a numerical implementation of the Kriging algorithm with an advanced search algorithm, developed for geophysical track line data (Herzfeld, Wallin, and Stachura 2012). Other Kriging methods have also been applied in analysis of altimeter data (but not CryoSat-2 data). For example, Stosius and Herzfeld (2004) implement a dynamic Kriging approach that uses locally changing variography for dierent surface provinces (derived from SAR data) to improve DEM estimation from satellite radar altimeter data. Hurkmans et al. (2012) use Kriging with external drift to create maps of Jakobshavn Isbræ (Ilulissat Icestream) from Airborne Topographic Mapper (ATM) laser altimeter data. However, the external drift variable requires ancillary data, as the name implies, hence this approach would not be suitable for assessment of the usefulness of the primary variable for DEM construction as in this study.

To facilitate analysis of elevation change based on the time series of maps, the same variogram model will be used in the estimation step for all six seasons. This employs the assumption that the spatial relationship with respect to each lag distance remains constant across data sets and is independent of the season.

In a separate study, a detailed variogram analysis was carried out for each one of the six 6-month intervals with the result that the variograms were similar to each other, with small differences between Winter and Summer surfaces. Therefore, using the same variogram for each season in this study is justified. We select the variogram from the Summer 2012 data set (Figure 3) due to its superior coverage (see Figure 2). The same variogram is used for all six-month data sets to ascertain that elevation differences are attributable to differences in height observations (and not partly to different variography, i.e. different interpolation operates). Following the approach described in Sections 3 and 4, six 200-by-200 m DEMs of Bering Glacier surface topography are derived for the summer and winter seasons between May 2011 and April 2014 (see Figure 5).

6. Error analysis

Two methods are applied to derive error maps for DEMs: (1) the standard deviation of the Kriging method and (2) error maps using a formula resultant from numerical error propagation through the Kriging equations. Method (1) is the standard method found in the Kriging literature (Journel and Huijbregts (1989); Matheron (1963)), method (2) is derived in Herzfeld (1992).

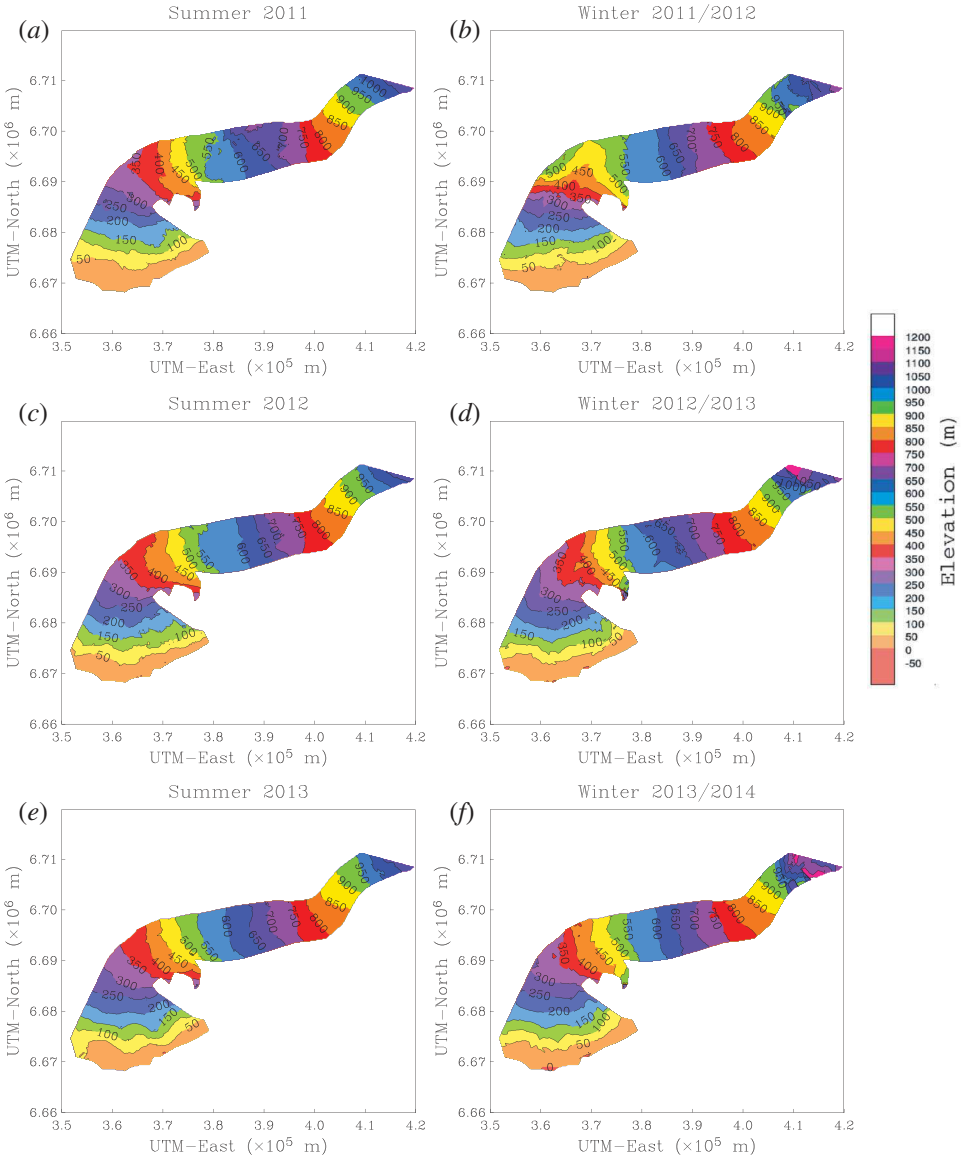

Figure 5. Bering Glacier surface elevation from CryoSat-2 data. Each colour represents a 50 m contour. (a) Summer 2011, (b) Winter 2011/2012, (c) Summer 2012, (d) Winter 2012/2013, (e) Summer 2013, and (f) Winter 2013/2014.

6.1. *Estimated standard deviation*

The estimation variance $s^2 = E\,[Z_0^* - Z_0]^2$ of OK is given by

$$s^2 = \sum_{i=1}^{n} a_i \gamma_{0,i} + \lambda, \tag{10}$$

where λ is a Lagrange multiplier used in solving the Kriging system. An advantage of the formula is that the estimation standard deviation (and variance) can be calculated without significant additional computational effort, because the coefficients α_i are derived by inverting the OK system. The estimation standard deviation is not an error measure in the sense of numerical error analysis, and rather depends only on the data distribution in space. Consequently, this error measure simply reflects the survey pattern (it is a combination of the distance to the nearest track, the variogram values and the weights). The estimation standard deviation maps for each season can be seen in Figure 6.

6.2. *Numerical error propagation*

The second method applies numerical random error propagation through the Kriging equations (Herzfeld 1992).

Theorem: Propagation of standard error through a function. If U is a quantity derived as a function $U(x_1, ..., x_n)$ of measured quantities $x_1, ..., x_n$ for a natural number n, then the standard deviation σ_U can be expressed in terms of the standard deviations σ_i of x_i for $i = 1, ..., n$ as follows:

$$\sigma_U = \sum_{i=1}^{n} \left(\frac{\partial U}{\partial x_i} \right)^2 {\sigma_i}^2. \tag{11}$$

The theorem is quoted after Moffitt and Bouchard (1992) (eqn. 4–16, p. 168). It should be noted that an analytical approach to error approximation, based on absolute errors, would yield a different result. The form of the error equation is the same (based on derivatives) in the analytical case.

In the following, the theorem is applied to the Kriging Equation (6), noting unbiasedness conditions (5) for ordinary Kriging. The procedure for the calculation of numerical error follows three steps:

(Step 1) Calculation of nugget values(c_0).

As a first step in creating error maps, nugget values are derived for variograms calculated in distance bins for each CryoSat-2 data point. The value in the first bin of the variogram is taken as the nugget value (the bin size is 300 m in this analysis).

(Step 2) Calculation of noise levels(σ_0).

Noise levels are derived from nugget values, for along-track bins. Since the (semi)variogram corresponds to half the variance for a certain distance class, the nugget is half the variance of observations in the same location, and hence the noise level, σ_0, is estimated as

$$\sigma_0 = \sqrt{2c_0}, \tag{12}$$

(Step 3) Calculation of numerical error (s_0).

An estimate of the Kriging (numerical) standard deviation is derived by propagating the noise levels through the Kriging calculations, using methods applicable to random error propagation, that is, by application of the Theorem using Equation (11). Application of the error propagation method to the Kriging estimator (Equation (3) with $\alpha_0 = 0$) gives

$${s_0}^2 = {\sigma_0}^2 \sum_{i=1}^{n} {\alpha_i}^2, \tag{13}$$

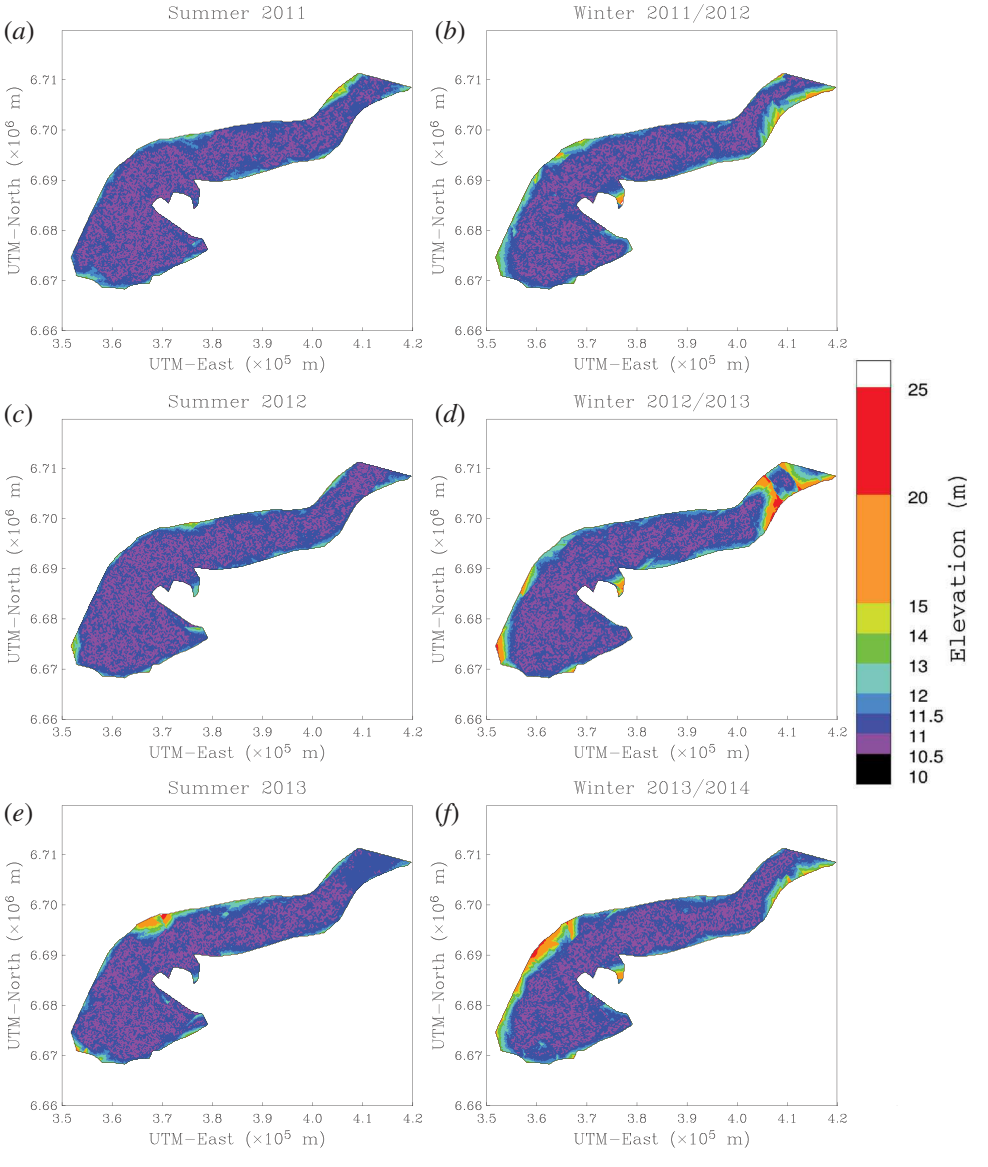

Figure 6. Kriging estimation standard deviation. (a) Summer 2011, (b) Winter 2011/2012, (c) Summer 2012, (d) Winter 2012/2013, (e) Summer 2013, and (f) Winter 2013/2014.

where s_0 is the error estimate associated with elevation $z(x_0)$ at location x_0, σ_0 is the average noise level in the neighbourhood of x_0 (as determined in step 2), and a_i ($i = 1, \ldots, n$) are the Kriging weights from OK, because

$$\frac{\partial Z_0^*}{\partial Z_i} = a_i. \tag{14}$$

For simplicity, the deviation of the numerical error assumes that the standard deviation of measurement is the same throughout the neighbourhood used for estimation of a point. Maps displaying the data coverage, noise levels, and error values for each

season can be seen in Figures 7 and 8, respectively, while a table displaying the mean and standard deviation of the nugget values, noise levels, and error values is Table 1.

6.3. *Results of error analysis*

6.3.1. *Kriging estimation standard deviation*

Maps in Figure 6 display an average estimation standard deviation of 11.32 ± 1.01 m throughout the glacier for all seasons (see Table 1 for error estimates for each individual season). Because this error measure reflects the data survey pattern, areas with low coverage, such as the upper glacier near the BBJ, have higher estimation standard deviation. In areas of low coverage the algorithm needs to search for points that are further away when estimating elevation and therefore uses points that have higher spatial variability (higher variogram values). The assumption of ordinary Kriging that ignores trends in the data is also amplified at larger separation distances. Using data sets that span shorter time periods (such as one or three months) would increase the estimation standard deviation due to decreased coverage leading to measures that are on average much higher than 11 m.

Higher estimation standard deviations also occur near the margins of the glacier. Elevation estimates use only points that are on the glacier and not on the surrounding landscape (except near the BBJ where measurements on the Bagley Ice Field were used in estimation). Hence, elevation estimates for grid nodes near the glacier margin will be based on data with larger separation distances and higher variogram values. There is also overall better coverage, and thus lower estimation standard deviation, in the Summer DEMs compared to the Winter DEMs. This is due in part to attenuation of the radar signal by the snow cover due to volume scattering, which in effect can reduce the number of retrievable points.

6.3.2. *Numerical error of Kriging*

Noise estimates and numerical error via noise propagation through the Kriging algorithm are shown in Figures 7 and 8, respectively, and summarized in Table 1. The average numerical Kriging error when considering all data points is 1.65 ± 3.19 m (Table 1). Note that this error measure is non-negative. Estimations of noise levels were made by calculating nugget values for every raw data point, as determined by the value of the first distance bin. We then document the effects of noise propagation through the Kriging method to estimate the numerical error of the algorithm. This estimation assumes uniform elevation within a 300 m radius and therefore any variation in this assumption is considered a result of noisy data. The effective noise used in our analysis exists through a combination of measurement error, actual surface roughness in that area, and/or elevation change that occurred *within* the six-month time frame of the data set.

The average numerical error is always less than the average noise level due to the Kriging algorithm's mitigating effect on noisy data through use of a variety of points for estimation. Average error levels range from 1.23 m (Winter 2013/2014) to 2.04 m (Summer 2012). Although Summer 2012 had the best coverage, it also had the noisiest data. This could be due to increased surge activity during this time, with significant elevation change and high surface roughness.

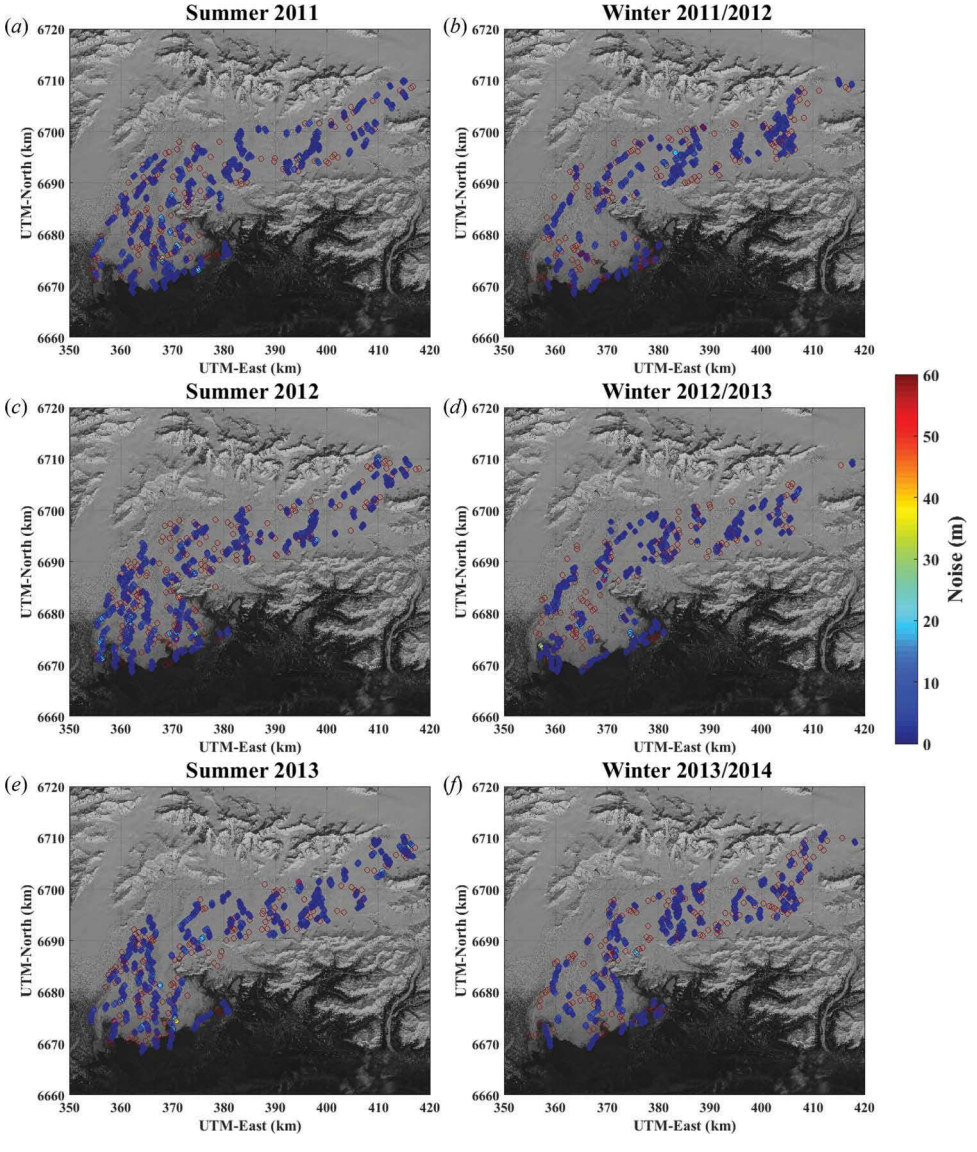

Figure 7. Estimated noise in the CryoSat-2 measurements derived from calculations of the nugget value. Points displayed as an empty red circle did not have any data points within a radius equal to the first distance bin and hence nugget values (and thus noise values) were not calculated there. (a) Noise Summer 2011, (b) noise Winter 2011/2012, (c) noise Summer 2012, (d) noise Winter 2012/2013, (e) noise Summer 2013 and (f) noise Winter 2013/2014. Background image from LandSat-8 acquired on 28 April 2013.

7. Comparison with airborne laser altimetry

To evaluate uncertainties in CryoSat-2 measurements, we perform a comparison with airborne laser altimeter data using crossover analysis. As part of observational campaigns conducted during the surge of the BBGS under a National Science Foundation (NSF) Grant for Rapid Response Research (RAPID), we collected airborne laser altimeter

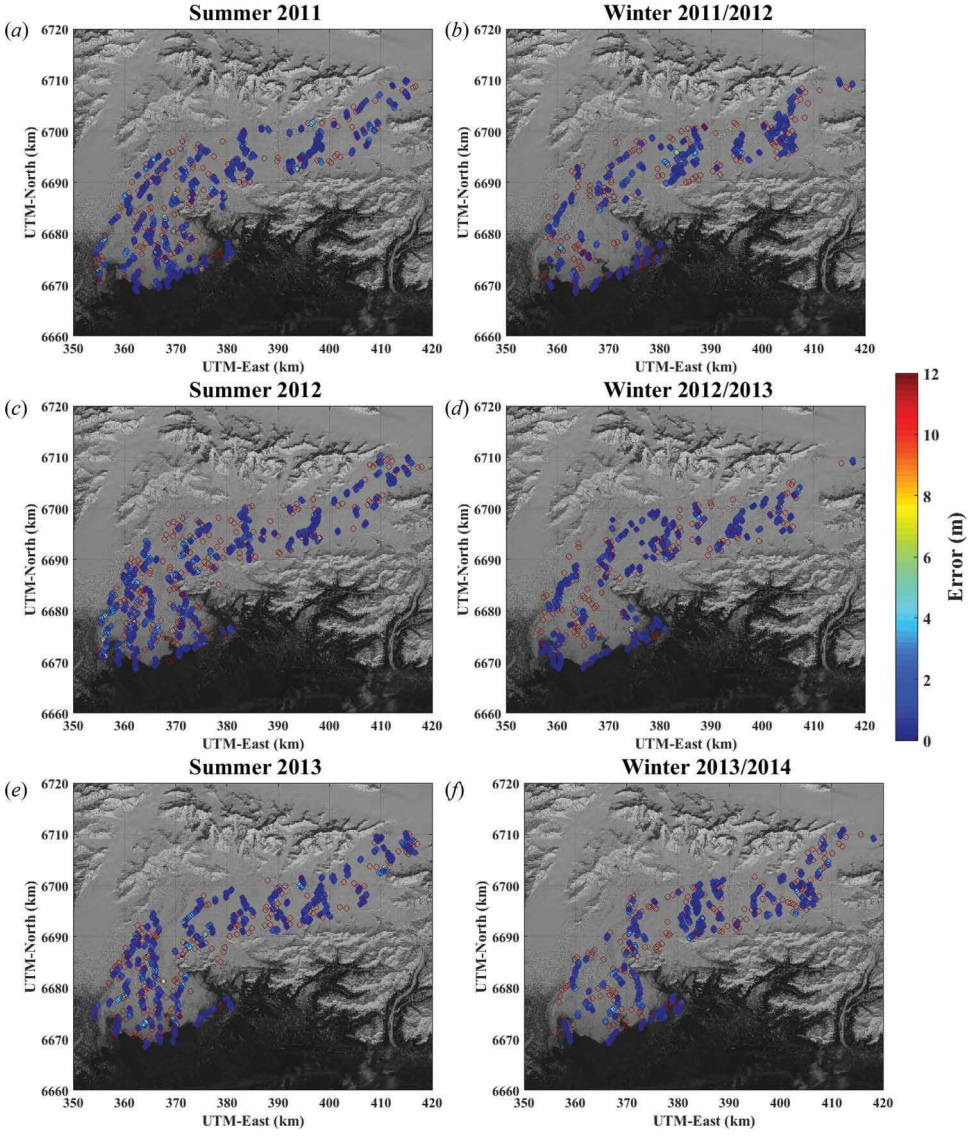

Figure 8. Numerical error from the propagation of the noise through the Kriging algorithm. Points displayed as an empty red circle did not have any data points within a radius equal to the first distance bin and hence nugget values (and thus error values) were not calculated there. (a) Error Summer 2011, (b) error Winter 2011/2012, (c) error Summer 2012, (d) error Winter 2012/2013, (e) error Summer 2013 and (f) error Winter 2013/2014. Background image from LandSat-8 acquired on 28 April 2013.

data, using the Universal Laser System (ULS) on (1) 25 and 26 September 2011, (2) 1 October 2012, and (3) 14 August 2013. The crossover analysis is based on the CryoSat-2 Summer data sets (May–October 2011, 2012, 2013) because all airborne campaigns were flown between mid-August and early October. The CryoSat-2 data used are those retained after the filtering algorithm described in Section 4.2.

Table 1. Error analysis means and standard deviations.

	Estimation standard deviation (m)	Kriging error (m)	Noise (m)	Nugget (m^2)
Summer 2011	11.15 ± 0.46	1.48 ± 1.93	4.33 ± 5.54	24.71 ± 98.88
Winter 2011/2012	11.33 ± 0.85	1.81 ± 4.53	5.32 ± 12.90	97.17 ± 619.98
Summer 2012	11.13 ± 0.41	2.07 ± 3.81	6.16 ± 11.53	85.27 ± 543.19
Winter 2012/2013	11.58 ± 1.57	1.78 ± 3.69	5.19 ± 10.78	71.46 ± 303.34
Summer 2013	11.25 ± 0.88	1.39 ± 2.26	4.06 ± 6.30	28.03 ± 141.95
Winter 2013/2014	11.47 ± 1.27	1.26 ± 2.02	3.63 ± 5.97	24.40 ± 140.11
All data	11.32 ± 1.01	1.65 ± 3.19	4.83 ± 9.31	54.99 ± 368.50

7.1. *Instrument description*

The ULS instrument, built by Laser Technology, Inc., is a single-beam nadir-pointing rangefinder that measured distance from the aircraft to the ground surface. It operates with a 905 nm (near-infrared) wavelength and a 400 Hz collection rate corresponding to a 7.5 cm along-track sample spacing when flown at 30 m s^{-1}. The ULS was coupled with a global positioning system (GPS) to produce horizontal coordinates for each elevation measurement. A full description of the instrument and observation process can be found in Crocker et al. (2011) and in Herzfeld et al. (2013c).

7.2. *Crossover analysis and interpretations*

For the crossover analysis we determine elevation differences between each CryoSat-2 data point and the average elevation of all airborne altimetry measurements, if any, within a 300 m radius. Average crossover differences from the three comparisons are consistently near 5 m with standard deviations ranging from 10 to 15 m (see Table 2). Note that these differences are expectedly similar to the noise estimates given in Table 1. Interpretations of the crossover analysis displayed in Figure 9 are summarized as follows:

For 2011, difference values appear to be clustered regionally. In the lower Tashalich Arm region (362 km E/6682 km N UTM), CryoSat-2 data are too low compared to ULS data by almost 20 m. During May–September 2011, mass was transferred downglacier in Tashalich Arm as part of the surge, following the collapse of a bulge upstream Herzfeld et al. (2013c). Hence the crossover differences may be attributable to actual height differences that evolved during this 6-month period.

For the same time period, the red points (10–25 m elevation gain) clustered over the southern branch of Bering Glacier in the vicinity of the Grindle corner (368 km E/6682 km N UTM) may suggest a thickening in this region. In contrast, the central Bering Glacier crossover values are consistently high, indicating that CryoSat-2 elevations are 5–25 m higher than ULS data.

Table 2. Crossover analysis means and standard deviations. C2 stands for CryoSat-2.

	C2 Summer 2011 – ULS Fall 2011	C2 Summer 2012 – ULS Fall 2012	C2 Summer 2013 – ULS Fall 2013	Total
Number of points	40	125	51	216
Elevation difference (m)	5.036 ± 15.851	4.990 ± 14.176	5.130 ± 10.462	5.032 ± 13.673

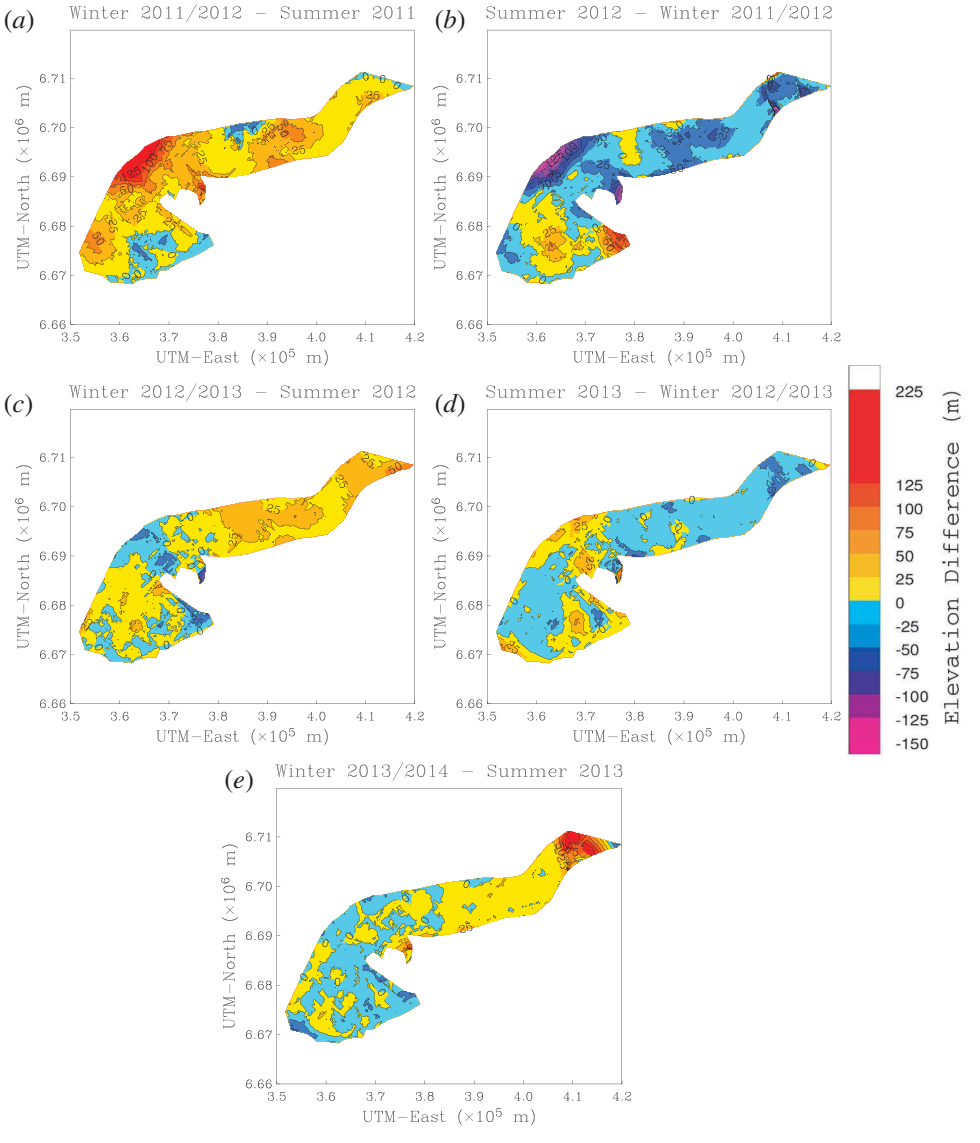

Figure 9. Time series of six-month surface elevation change of Bering Glacier spanning Summer 2011 to Winter 2013/2014. (a) Winter 2011/2012 minus Summer 2011, (b) Summer 2012 minus Winter 2011/2012, (c) Winter 2012/2013 minus Summer 2012, (d) Summer 2013 minus Winter 2012/2013, and (e) Winter 2013/2014 minus Summer 2013.

Along the southern branch of Bering Glacier, measurements in Fall 2012 are within ± 5 m, with CryoSat-2 surface heights slightly higher than ULS surface heights. This is the area of largest activity in 2012.

For 2013 the standard deviations are lower (10 m) than for the previous two years (15.8 and 14.1 m), which can potentially be related to the fact that in 2013 the surge had progressed into the Bagley Ice Field, while Bering Glacier started to return to quiescent

state. Crevasses fields age, which is accompanied by decrease of surface roughness, increase of roundedness of crevasse ages and decreasing crevasse depth.

7.3. *Relationships of CryoSat-2 accuracy to crevasse fields*

The CryoSat-2 surface heights appear to be generally too low over crevasse fields. Examples are seen over a crevasse field located at 363 km E/6684 km N in the 2011 and 2012 data analysis (Figure 9(a,b)). This is likely a result of forward scattering (range delay) over rough areas, as the SIRAL signal may get delayed in crevasses before returning to the receiver. An analogous effect was observed for GLAS data Herzfeld et al. (2013a). In contrast, the ULS registers surface heights inside crevasses and between crevasses accurately (as determined in Herzfeld et al. (2013c)), because data are collected over a much shorter range (typically 500 meters) and with a spatial resolution of typically 0.75 m along-track. In other crevassed areas, there is no systematic relationship.

8. Results and interpretation

8.1. *CryoSat-2 data as a means for deriving DEMs*

As derived in the error analysis section, CryoSat-2 data can be employed to map surface elevations of Bering Glacier, Alaska. Consequently, CryoSat-2 can be used to map elevation in other large mountain glaciers. (Bering Glacier is approximately 80 km in length and ranges in width from about 8 km in the upper glacier to over 20 km in the glacier lobus). Elevation maps were created for the six-month time intervals of Summer 2011 (May–October), Winter 2011/2012 (November–April), Summer 2012, Winter 2012/13, Summer 2013 and Winter 2013/2014.

8.2. *CryoSat-2 data as a means for estimating elevation change*

CryoSat-2 data can be used to derive elevation change during the surge of Bering Glacier in 2011–2014 (see Figures 10 and 11). More generally, our results indicate that the accuracy and spatial resolution of CryoSat-2 data is sufficient to reveal large (tens of metres) and rapid elevation changes and mass transfers in large mountain glaciers, ice streams and outlet glaciers of the large ice sheets.

Here, large changes mean tens of metres in height change, rapid changes refer to changes that may occur over as little as six months, or over longer time periods. The limiting factor for a physically useful CryoSat-2 data analysis lies in the amount of data covered per time. Hence changes on the order of 10 m or more can be detected over longer time intervals, whereas time intervals shorter than six months were not determined to yield sufficient coverage for DEM calculation or crossover analysis.

8.3. *Results of crossover analysis*

Comparison of Summer (May–October) CryoSat-2 data with airborne laser altimeter data indicates a generally good correspondence (approximately 5 m average crossover differences with 15.9 m (2011), 14.2 m (2012), and 10.5 m (2013) standard deviations).

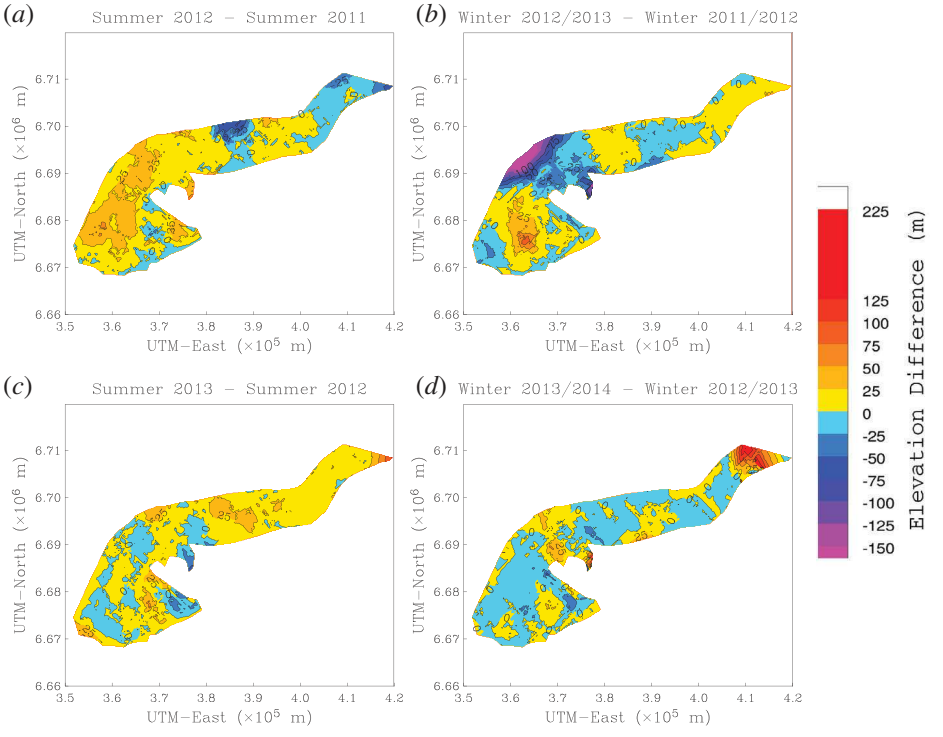

Figure 10. One-year surface elevation change of Bering Glacier. (a) Summer 2012 minus Summer 2011, (b) Winter 2012/2013 minus Winter 2011/2012, (c) Summer 2013 minus Summer 2012, and (d) Winter 2013/2014 minus Winter 2012/2013.

Two components emerged in the interpretation of differences: (1) Part of the elevation differences may be attributable to actual elevation changes that occurred in the Bering Glacier System during the surge in 2011–2013. (2) Discrepancies exist over crevasse fields, where CryoSat-2 data are mostly lower than ULS data. This is likely a result of range delay in the CryoSat-2 data, while ULS data map crevasse profiles because of their high spatial resolution.

8.4. *Interpretation of difference maps for Bering Glacier 2011–2014*

Elevation change maps were created for each six-month interval and each annual interval (see Figure 10). These maps reveal several of the physical processes that occurred during the surge:

Elevation change maps for the interval Summer 2011 to Winter 2011/2012 (Figure 10 (a,b)) reveal a mass transfer from an area in northern central Bering Glacier down-glacier. This mass transfer is associated with the collapse of a large reservoir area that has formed during the quiescent phase and marks the initiation of a surge or surge phase. An earlier stage of this event was also observed during field campaigns and is reported in Herzfeld et al. (2013c). Elevation change from airborne laser altimeter data was measured as 70 m surface height loss in the reservoir area and 20–40 m surface height increase in an area downstream. These results use differences between 2010 airborne

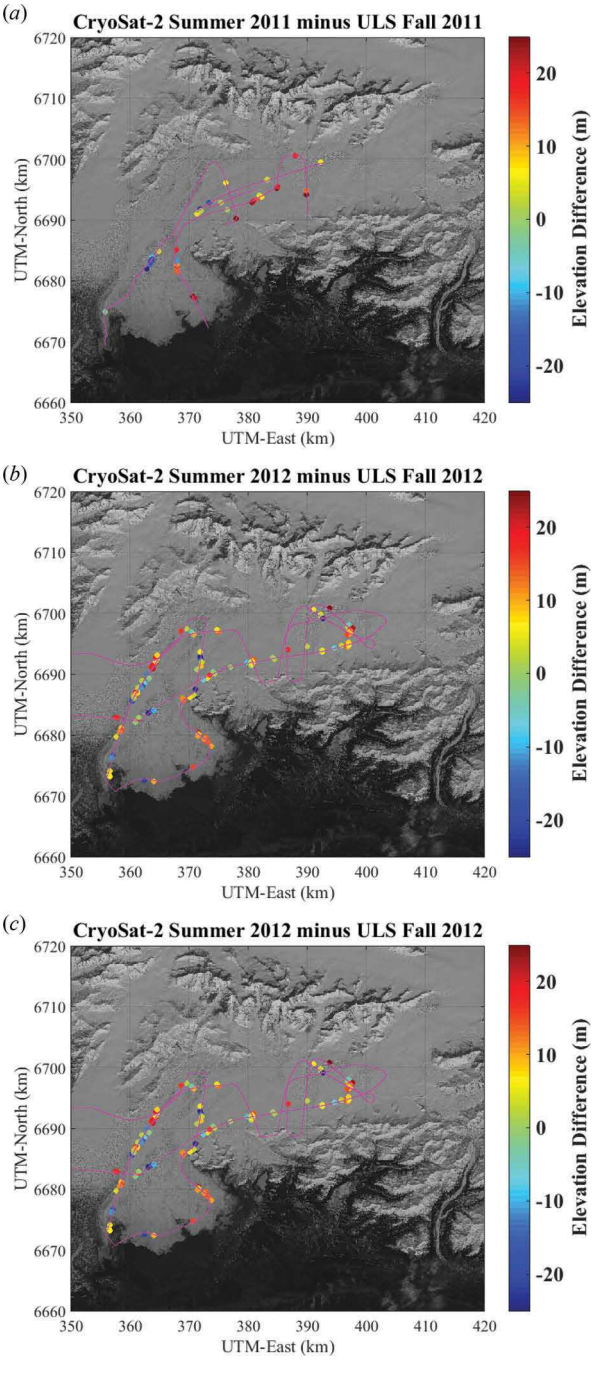

Figure 11. Elevation differences in measurements by CryoSat-2 (over a six-month period) and ULS airborne altimeter data sets. Flight tracks of the ULS airborne campaigns over Bering Glacier are in magenta. (a) CryoSat-2 Summer 2011 data set minus ULS data set from 25 and 26 September 2011, (b) CryoSat-2 Summer 2012 data set minus ULS data set from 1 October 2012, and (c) CryoSat-2 Summer 2013 data set minus ULS data set from 14 August 2013. Background image from LandSat-8 acquired on 28 April 2013.

altimeter data collected as part of NASA's Operation IceBridge (Alaska part) and airborne altimeter data collected in September 2011 by U. Herzfeld (Bering Glacier NSF RAPID Campaign). The CryoSat-2 difference maps show a continuation and further expansion of this mass transfer. The mass transfer appears to be largely restricted to the northern branch of Bering Glacier (Tashalich Arm). The positive signal near 395 km E/6695 km N UTM may be attributed to changes in the area of a large rift, which has a complex development (see Herzfeld, McDonald, and Weltman (2013b, 2013c)).

The difference maps for the following six-month intervals show mass transfer to the lobus area until Winter 2012/2013. The initiation of the 2012 surge phase, that affected the longitudinally southern branch of Bering Glacier, as evident in airborne observations during July 2012 and October 2012, may correspond to the fact that a longitudinal separation in elevation change exists in the first two maps (*a*), (*b*), but not for the maps from later seasons (*c*), (*d*), (*e*).

The last difference map (Figure 10(e)) indicates a start of the return to quiescent state with thinning in the lower glacier (lobus) and part of lower-central Bering Glacier. The high elevation change in the eastern corner of Bering Glacier is not an artefact of Kriging nor an edge effect. The location where this change occurs is a large icefall at the junction of Bering Glacier and Bagley Ice Field that has been affected by surge crevassing throughout the surge years. In 1995, the final year of the previous surge, the surge wave propagated into the Bagley Ice Field (Herzfeld and Mayer 1997). An interpretation of the physical processes at the BBJ, however, will require investigation of a larger area.

Elevation change maps derived for 1-year differences (Figure 11) similarly indicate processes observed in the field. Note that only large elevation changes are interpreted, while small changes may be attributed to noise/errors (see error analysis in Section 8) together with snowfall, wind re-deposition and melting.

9. Summary

Altimeter data from the European Space Agency's Earth Explorer Mission CryoSat-2 are analysed and interpreted towards four objectives: (1) mapping surface elevation of Bering Glacier, Alaska, through derivation of a time series of digital elevation models; (2) a complete error analysis justifying geophysical interpretations using CryoSat-2 derived DEMs in large mountain glaciers; (3) comparison with airborne laser altimetry and cross-over analysis; and (4) derivation of elevation-change maps to study the physical processes that occurred in the latest surge of Bering Glacier in 2011–2013.

This study uses SIRAL SARIn mode data, processed to the level L2 by ESA (Baseline B processing form), to derive surface elevation maps of Bering Glacier from Summer 2011 to Winter 2013/2014, where it is determined that a minimum of 6 months of consecutive CryoSat-2 observations are required to create a geophysically meaningful map. Ordinary Kriging is used to derive Digital Elevation Models of the Bering Glacier ice surface. Three methods of error analysis are applied: (1) the estimated standard deviation of Kriging; (2) effective measurement noise through calculation of nugget values; and (3) the propagation of this noise through the Kriging algorithm (numerical error). Resultant DEMs have an average estimation standard deviation of 11.32 ± 1.01 m resulting from data coverage (or lack thereof), and average numerical error of 1.65 ± 3.19 m due to algorithmic propagation of noise induced by effects of actual measurement, data processing and assumptions on the

data set. The estimation standard deviation, which depends on the survey pattern, dominates the error over effects of noise. For evaluation of CryoSat-2 data accuracy, a comparison with airborne laser altimeter data was undertaken. These data were collected during fall 2011, 2012, and 2013 as part of the second author's NSF-funded Bering Glacier Surge Project. The correspondence is generally good with differences of 5.032 ± 13.673 m. Systematic differences in CryoSat-2 and airborne altimeter data are due to elevation changes during the surge (2011–2013) and to the influence of surface roughness, especially over crevasse fields.

As a result, the time series of DEMs derived from CryoSat-2 L2 data products can be used to map elevations of Bering Glacier and other mountain glaciers or glacier systems of similar size or width. The Bering Glacier DEMs have also seen immediate use in numerical modelling (Trantow 2014). Aside from serving as model inputs that describe initial glacier geometry, the time series of these DEMs may serve as a validation measure for numerical simulations of elevation change and surface mass balance.

Because elevation changes during the surge were on the order of 20–70 m between 2010 and 2011 (Herzfeld et al. 2013c), the time series can also be used to study elevation changes. Elevation change maps reveal several physical processes that mark the progression of the surge: (a) The collapse of an elevation bulge, the reservoir area, that formed during quiescent phase. The bulge collapse marks the start of a surge phase. (b) Mass transfer during the surge, first limited to the northern branch of Bering Glacier (Tashalich Arm), then extending across large areas of the glacier. Details cannot be derived from CryoSat-2 data analysis, due to lack of resolution and coverage. (c) Thickening in the lobus area during 2011 and 2012, then return to thinning in the lobus area by 2014 marking a return to quiescence.

These processes have also been observed in aerial laser altimeter data, video, and GPS data. Therefore, our aerial observations and process analysis provide a validation of large signals that have been derived from CryoSat-2-based DEMs in this article. For Bering Glacier, the CryoSat-2 data analysis yields a time series of elevation and elevation-change DEMs, whereas the airborne data only resulted in elevation data along-tracks. The result of this validation is that CryoSat-2 data can indeed be employed for DEM-calculation that warrant interpretation of large elevation changes in mountain glaciers.

Acknowledgements

Thanks are due to Brian McDonald, CU Boulder, for help with data processing, and to Enrica Cocco, EO Help Desk, for discussion of cross-track geolocation and phase-wrapping errors of CryoSat-2 data. Support for this work through U.S. National Science Foundation Arctic Natural Sciences Awards "RAPID Bering Glacier Surge 2011: Observation, Analysis and Parametrization" (NSF-ANS 1548462), "Bering Glacier Research Experience for Undergraduates" (NSF-ANS 1549750), NSF Geography and Spatial Sciences Award "A Surge in a Complex Glacier System: Results from Observations, Data Analysis and Numerical Experiments of the Bering-Bagley Glacier System" (NSF-GSS 1553133), and NASA Cryospheric Sciences Award "Study of Glacial Acceleration Types Through Innovative Approaches to CryoSat-2, ICESat Operation IceBridge and Other Altimeter Data Analysis" (NNX15AC73G) is gratefully acknowledged. Airborne ULS data collected during the Bering Glacier RAPID project are available via ACADIS at https://www.aoncadis.org/project/Bering_Glacier_Surge.html.

Disclosure statement

No potential conflict of interest was reported by the authors.

Funding

This work was supported by U.S. National Science Foundation Arctic Natural Sciences Awards "RAPID Bering Glacier Surge 2011: Observation, Analysis and Parametrization" [NSF-ANS 1548462], "Bering Glacier Research Experience for Undergraduates" [NSF-ANS 1549750], NSF Geography and Spatial Sciences Award "A Surge in a Complex Glacier System: Results from Observations, Data Analysis and Numerical Experiments of the Bering-Bagley Glacier System" [NSF-GSS 1553133], and NASA Cryospheric Sciences Award "Study of Glacial Acceleration Types Through Innovative Approaches to CryoSat-2, ICESat Operation IceBridge and Other Altimeter Data Analysis" [NNX15AC73G].

References

Bamber, J. L., S. Ekholm, and W. B. Krabill 2001. "A New, High-Resolution Digital Elevation Model of Greenland Fully Validated with Airborne Laser Altimeter Data." *Journal of Geophysical Research: Solid Earth (1978–2012)* 106 (B4): 6733–6745. doi:10.1029/2000JB900365.

Biau, G., E. Zorita, H. von Storch, and H. Wackernagel 1999. "Estimation of Precipitation by Kriging in the Eof Space of the sea Level Pressure Field." *Journal of Climate* 12 (4): 1070–1085. doi:10.1175/1520-0442(1999)012<1070:EOPBKI>2.0.CO;2.

Bouffard, J. 2015. *CRYOSAT-2: Level 2 Product Evolutions and Quality Improvements in Baseline C (V3)*. Paris: European Space Agency.

Clarke, G. 1987. "Fast Glacier Flow: Ice Streams, Surging, and Tidewater Glaciers." *Journal of Geophysical Research* 92: 8835–8842. doi:10.1029/JB092iB09p08835.

Crocker, R. I., J. A. Maslanik, S. E. Palo, J. J. Adler, U. C. Herzfeld, and W. J. Emery 2011. "A Sensor Package for Ice Surface Characterization Using Small Unmanned Aircraft Systems." *IEEE Transactions Geosc Remote Sensing* 49 (99): 1–15.

Curran, P. J. 1988. "The Semivariogram in Remote Sensing: An Introduction." *Remote Sensing of Environment* 24 (3): 493–507. doi:10.1016/0034-4257(88)90021-1.

Drinkwater, M., R. Francis, G. Ratier, and D. Wingham 2004. "The European Space Agency's Earth Explorer Mission CryoSat: Measuring Variability in the Cryosphere." *Annals of Glaciology* 39: 313–320. doi:10.3189/172756404781814663.

ESA, E. S. A. 2007. *CryoSat Mission and Data Description (MDD)*, 82. Noordwijk: European Space Research and Technology Centre.

Galin, N., D. J. Wingham, R. Cullen, M. Fornari, W. H. Smith, and S. Abdalla 2013. "Calibration of the Cryosat-2 Interferometer and Measurement of Across-Track Ocean Slope." *Geoscience and Remote Sensing, IEEE Transactions on* 51 (1): 57–72. doi:10.1109/TGRS.2012.2200298.

Gardner, A. S., G. Moholdt, J. G. Cogley, B. Wouters, A. A. Arendt, J. Wahr, E. Berthier et al. 2013. "A Reconciled Estimate of Glacier Contributions to Sea Level Rise: 2003 to 2009." *Science* 340 (6134): 852–857. doi:10.1126/science.1234532.

Gray, L., D. Burgess, L. Copland, R. Cullen, N. Galin, R. Hawley, and V. Helm 2013. "Interferometric Swath Processing of Cryosat Data for Glacial Ice Topography." *The Cryosphere* 7 (6): 1857–1867. doi:10.5194/tc-7-1857-2013.

Gray, L., D. Burgess, L. Copland, M. Demuth, T. Dunse, K. Langley, and T. Schuler 2015. "Cryosat-2 Delivers Monthly and Inter-Annual Surface Elevation Change for Arctic Ice Caps." *The Cryosphere* 9 (5): 1895–1913. doi:10.5194/tc-9-1895-2015.

Harrison, W., and A. Post 2003. "How Much Do We Really Know about Glacier Surging?" *Annals of Glaciology* 36 (1): 1–6. doi:10.3189/172756403781816185.

Helm, V., A. Humbert, and H. Miller 2014. "Elevation and Elevation Change of Greenland and Antarctica Derived from Cryosat-2." *The Cryosphere Discussions* 8: 1673–1721. doi:10.5194/tcd-8-1673-2014.

Herzfeld, U. 1989. "Geostatistical Methods for Evaluation of Seabeam Bathymetric Surveys: Case Studies of Wegener Canyon, Antarctica." *Marine Geology* 88 (1–2): 83–95. doi:10.1016/0025-3227(89)90006-6.

Herzfeld, U. 1992. "Least-Squares Collocation, Geophysical Inverse Theory and Geostatistics: A Bird's Eye View." *Geophysical Journal International* 111 (2): 237–249. doi:10.1111/gji.1992.111.issue-2.

Herzfeld, U., C. Lingle, and L. Lee 1993. "Geostatistical Evaluation of Satellite Radar Altimetry for High Resolution Mapping of Antarctic Ice Streams." *Annals Glaciol* 17: 77–85.

Herzfeld, U., B. McDonald, B. Wallin, W. Krabill, S. Manizade, J. Sonntag, H. Mayer, W. Yearsley, P. Chen, and A. Weltman 2013a. "Dynamic Provinces of Jakobshavn Isbræ Derived from Generalized Spatial Surface Roughness." *Journal of Glaciology* 60 (223): 834–848.

Herzfeld, U., B. McDonald, and A. Weltman 2013b. "Bering Glacier and Bagley Ice Valley Surge 2011: Crevasse Classification as an Approach to Map Deformation Stages and Surge Progression." *Annals of Glaciology* 54 (63): 279–286. doi:10.3189/2013AoG63A338.

Herzfeld, U., B. Wallin, and M. Stachura 2012. "Applications of Geostatistics in Optimal Design of Satellite Altimetry Orbits and Measurement Configurations." *Journal of the Astronautical Sciences* 58 (3): 495–511. doi:10.1007/BF03321182.

Herzfeld, U. C. 2002. "Vario Functions of Higher Order–Definition and Application to Characterization of Snow Surface Roughness." *Computers & Geosciences* 28 (5): 641–660. doi:10.1016/S0098-3004(01)00096-6.

Herzfeld, U. C. 2004. *Atlas of Antarctica: Topographic Maps from Geostatistical Analysis of Satellite Radar Altimeter Data*. Vol. 1. Berlin: Springer Verlag.

Herzfeld, U. C., and H. Mayer 1997. "Surge of Bering Glacier and Bagley Ice Field, Alaska: An Update to August 1995 and an Interpretation of Brittle-Deformation Patterns." *Journal of Glaciology* 43 (145): 427–434.

Herzfeld, U. C., B. McDonald, M. Stachura, R. G. Hale, P. Chen, and T. Trantow 2013c. "Bering Glacier Surge 2011: Analysis of Laser Altimeter Data." *Annals of Glaciology* 54 (63): 158–170. doi:10.3189/2013AoG63A348.

Hurkmans, R., J. Bamber, L. S. Srensen, I. Joughin, C. Davis, and W. Krabill. 2012. "Spatiotemporal Interpolation of Elevation Changes Derived from Satellite Altimetry for Jakobshavn Isbr, Greenland." *Journal of Geophysical Research: Earth Surface* 117 (F3). doi:10.1029/2011JF002072.

Journel, A., and C. Huijbregts 1989. *Mining Geostatistics*. 2nd ed. London: Academic Press.

Lee, H., C. Shum, K. Tseng, Z. Huang, and H. Sohn 2013. "Elevation Changes of Bering Glacier System, Alaska, from 1992 to 2010, Observed by Satellite Radar Altimetry." *Remote Sensing of the Environment* 132: 40–48. doi:10.1016/j.rse.2013.01.007.

Matheron, G. 1963. "Principles of Geostatistics." *Economic Geology* 58 (8): 1246–1266. doi:10.2113/gsecongeo.58.8.1246.

McMillan, M., A. Shepherd, N. Gourmelen, A. Dehecq, A. Leeson, A. Ridout, T. Flament et al. 2014. "Rapid Dynamic Activation of a Marine-Based Arctic Ice Cap." *Geophysical Research Letters* 41 (24): 8902–8909. doi:10.1002/2014GL062255.

Meier, M. 1984. "Contribution of Small Glaciers to Global Sea Level." *Science* 226 (4681): 1418. doi:10.1126/science.226.4681.1418.

Meier, M., and A. Post 1969. "What are Glacier Surges?" *Canadian Journal of Earth Sciences* 6 (4): 807–817. doi:10.1139/e69-081.

Moffitt, F. H., and H. Bouchard. 1992. *Surveying*. New York: HarperCollins.

Molnia, B., and A. Post 1995. "Holocene History of Bering Glacier, Alaska: A Prelude to the 1993-1994 Surge." *Physical Geography* 16 (2): 87–117.

Molnia, B. F. 2008. *Alaska. Satellite Image Atlas of Glaciers of the World*. Washington, D.C: U.S. Geological Survey Professional Paper 1386-K.

Raymond, C. 1987. "How Do Glaciers Surge? A Review." *Journal of Geophysical Research* 92 (B9): 9121–9134. doi:10.1029/JB092iB09p09121.

Schutz, B., H. Zwally, C. Shuman, D. Hancock, and J. DiMarzio 2005. "Overview of the ICESat Mission." *Geophysical Research Letters* 32 (21). doi:10.1029/2005GL024009.

Stocker, T. F., H. Qin, G.-K. Plattner, M. Tignor, S. K. Allen, J. Boschung, A. Nauels, Y. Xia, V. Bex, and P. M. E. Midgley 2013. *Climate Change 2013: The Physical Science Basis. Contribution of Working Group I to the Fifth Assessment Report of the Intergovernmental Panel on Climate Change*. Cambridge: Cambridge University Press.

Stosius, R., and U. Herzfeld 2004. "Geostatistical Estimation from Radar Altimeter Data with respect to Morphologic Units Outlined by SAR Data - Application to Lambert Glacier/Amery Ice Shelf." *Annals of Glaciology* 39: 251–255. doi:10.3189/172756404781814159.

Tangborn, W. 2013. "Mass Balance, Runoff and Surges of Bering Glacier, Alaska." *The Cryosphere* 7 (3): 867–875. doi:10.5194/tc-7-867-2013.

Trantow, T. 2014. "Numerical experiments of dynamical processes during the 2011-2013 surge of the Bering-Bagley Glacier System, using a full-Stokes finite element model." Master's thesis., University of Colorado.

Truffer, M., and K. A. Echelmeyer 2003. "Of Isbrae and Ice Streams." *Annals of Glaciology* 36 (1): 66–72. doi:10.3189/172756403781816347.

Wingham, D., L. Phalippou, C. Mavrocordatos, and D. Wallis 2004. "The Mean Echo and Echo Cross-Product from a Beamforming Interferometric Altimeter and Their Application to Elevation Measurements." *IEEE Transactions on Geoscience and Remote Sensing* 42 (10): 2305–2323. doi:10.1109/TGRS.2004.834352.

Wingham, D. J., C. R. Francis, S. Baker, C. Bouzinac, R. Cullen, P. De Chateau-Thierry, S. W. Laxon, et al. 2006. "CryoSat: A Mission to Determine the Fluctuations in Earth's Land and Marine Ice Fields." *Advances in Space Research* 17 (4): 841–871.

Zwally, H., M. Giovinetto, J. Li, H. Cornejo, M. Beckley, A. Brenner, J. Saba, and D. Yi 2005. "Mass Changes of the Greenland and Antarctic Ice Sheets and Shelves and Contributions to Sea-Level Rise: 1992–2002." *Journal of Glaciology* 51 (175): 509–527. doi:10.3189/172756505781829007.